1-1-2001

Kinematics of Molecular Hydrogen Emission from Pre-Planetary Nebulae: RAFGL 2688 and RAFGL 618

Joel Kastner
Rochester Institute of Technology

David Weintraub
Vanderbilt University

Ian Gatley
Rochester Institute of Technology

LeeAnn Henn
Massachusetts Institute of Technology

Recommended Citation
Joel H. Kastner et al 2001 ApJ 546 279 https://doi.org/10.1086/318229

THE ASTROPHYSICAL JOURNAL, 546:279–287, 2001 January 1

KINEMATICS OF MOLECULAR HYDROGEN EMISSION FROM PRE–PLANETARY NEBULAE: RAFGL 2688 AND RAFGL 618

JOEL H. KASTNER,[1] DAVID A. WEINTRAUB,[2] IAN GATLEY,[1] AND LEEANN HENN[3]

Received 2000 February 11; accepted 2000 August 21

ABSTRACT

We present high spectral resolution maps of near-infrared molecular hydrogen emission from the bipolar pre–planetary nebulae RAFGL 2688 and RAFGL 618, obtained with the NOAO Phoenix spectrometer. The measured velocity gradients along the polar axes of both nebulae indicate that the highest velocity gas lies closest to the central stars. These results support the suggestion that the polar H_2 emission regions of both nebulae contain shocked gas formed as fast ($\sim$50–150 km s^{-1}), collimated, post–asymptotic giant branch (AGB) winds collide with slower moving ($\sim$10–20 km s^{-1}) material previously ejected while the central stars were still on the AGB. The kinematics of H_2 emission perpendicular to the polar axis of RAFGL 2688 are consistent with a model combining expansion along the equator at 5–10 km s^{-1} with rotation about the polar axis at 5–10 km s^{-1}. The rapid onset of the common envelope phase of a close binary system may explain both the bipolar structure of RAFGL 2688 and the presence and complex kinematics of its shocked H_2 emission.

Subject headings: dust, extinction — infrared: stars — ISM: individual (RAFGL 2688, RAFGL 618) — stars: AGB and post-AGB — stars: mass loss

1. INTRODUCTION

The bulk of the mass lost by stars of initial mass $\sim$1–8 $M_\odot$ is shed while such stars are on the asymptotic giant branch (AGB). Evidence is fast accumulating that, during late AGB or post-AGB evolutionary stages, the mass-loss geometry of such stars changes from more or less spherically symmetric to axially symmetric, with the result that the vast majority of planetary nebulae (PNs)—the endpoints of post–main-sequence stellar evolution for intermediate-mass stars—exhibits axisymmetric structures, ranging from elliptical to bipolar (see, e.g., reviews compiled by Kastner, Soker, & Rappaport 2000). Planetaries in the latter structural category are very likely to possess molecular envelopes (presumably the remnants of the ejected AGB envelope) that are readily detectable in the near-infrared rovibrational lines of H_2 (Kastner et al. 1996). The available data suggest, furthermore, that the onset of near-infrared H_2 emission in PNs can be traced back to the pre–planetary nebula (PPN) phase but not back to the AGB phase of evolution (Weintraub et al. 1998). These observations suggest that further studies of H_2 emission from PPNs and PNs may offer insight into the transition from AGB star to PN and from spherical to axisymmetric mass loss.

The Egg Nebula (RAFGL 2688; Ney et al. 1975) is perhaps the best-known example of such a transition object. Recent *Hubble Space Telescope* (*HST*) optical and near-infrared images of the Egg reveal a striking juxtaposition of circularly and axially symmetric structures (Sahai et al. 1998a, 1998b). This puzzling combination of structures has been detected in *HST* images of several other PPNs and PNs (see, e.g., reviews compiled by Kastner et al. 2000). An outstanding feature of RAFGL 2688, however, is the "quadrapolar" morphology of 2.122 μm H_2 emission detected in near-infrared images (Gatley, Depoy, & Fowler 1988); this structure is seen most clearly in an *HST*/NICMOS image (Fig. 1; Sahai et al. 1998a). This image shows that the linear extents and bow-shock–like structures of the polar and equatorial plane H_2 emission regions are very similar, suggesting a common origin. Furthermore, the sharp, limb-brightened boundaries of the H_2 emission in all four "lobes" is suggestive of a fairly sudden event in the object's recent past.

The kinematics of molecular emission from RAFGL 2688 have been the subject of numerous investigations. Bieging & Rieu (1988, 1996) and Cox et al. (2000) mapped the velocity distribution of rotational emission of various species with radio interferometers, and Cox et al. (1997) imaged near-infrared rovibrational H_2 emission at moderate velocity resolution. Radio interferometric observations of HCN by Bieging & Rieu yielded the rather surprising result of velocity gradients both along and perpendicular to the polar axis of the system, a result confirmed by Cox et al. These gradients, which are of similar magnitude, were interpreted by Bieging & Rieu (1988, 1996) as arising out of a combination of spherical expansion and rotation about the polar axis. Cox et al. (1997, 2000) and Lucas, Cox, & Huggins (2000), however, intepret the H_2 kinematics of RAFGL 2688 in terms of a system of multiple jets.

The evolved bipolar nebula RAFGL 618 (Westbrook et al. 1975) might be considered the direct evolutionary descendent of RAFGL 2688 in many respects. Both objects display molecule-rich circumstellar envelopes, carbon-rich circumstellar chemistries, and dusty, bipolar reflection nebulosities. Whereas RAFGL 2688 harbors an F-type central star and is not known to contain an H II region, RAFGL 618 possesses a B-type central star and compact H II region, suggesting that the latter nebula has evolved farther toward the PN stage. Like the Egg Nebula, RAFGL 618 displays bright near-infrared H_2 emission, but in the case of RAFGL 618, the H_2 emission appears to be confined to a region along its polar axis (Latter et al. 1995).

While the "quadrapolar" structure of the H_2 emission in the Egg appears to be unique, it may be a short-lived evolu-

[1] Chester F. Carlson Center for Imaging Science, Rochester Institute of Technology, 54 Lomb Memorial Drive, Rochester, NY 14623-5604; jhk@cis.rit.edu.

[2] Department of Physics and Astronomy, Vanderbilt University, P.O. Box 1807 Station B, Nashville, TN 37235.

[3] Center for Space Research, Massachusetts Institute of Technology, NE80-6007, Cambridge, MA 02139.

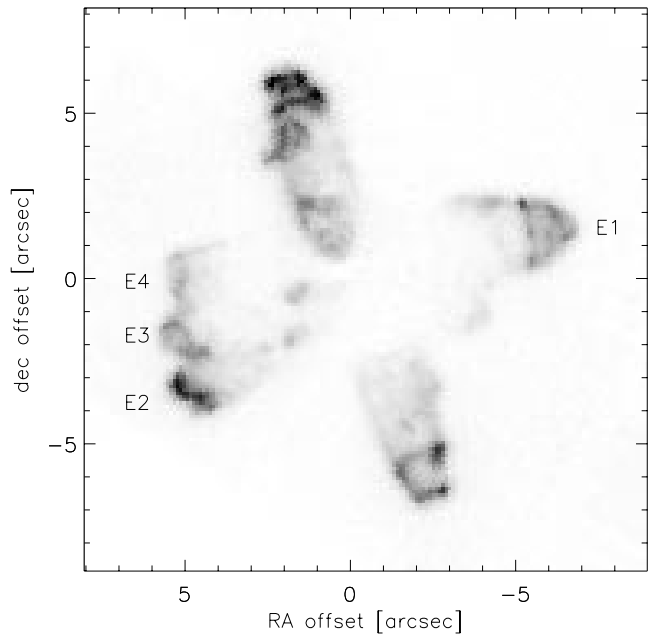

FIG. 1.—*HST*/NICMOS image of 2.12 μm H_2 emission from RAFGL 2688 (Sahai et al. 1998a). Features identified E1–E4 by Sahai et al. are indicated.

tionary phase common to many or most AGB stars as they go through the transition to PPNs. In RAFGL 618, however, the H_2 morphology also is unusual, as emission is found only along the polar axes, whereas most PNs in which H_2 is detected exhibit the strongest H_2 along the equatorial plane (Kastner et al. 1996). Thus, the kinematics and morphology of H_2 emission from these two objects are strongly deserving of more careful study. To investigate the H_2 velocity gradients of RAFGL 2688 in detail, we obtained a series of high-resolution, long-slit spectra in the 2.12 μm region with the NOAO[4] Phoenix near-infrared spectrometer (Hinkle et al. 1998). We also obtained a Phoenix spectrum of 2.12 μm H_2 emission from RAFGL 618. As we now describe, examination and comparison of the H_2 kinematics of these two objects, as revealed in the Phoenix spectroscopic data, offer clues to their detailed structures and recent evolutionary histories.

2. OBSERVATIONS

Data presented here were obtained with Phoenix on the 2.1 m telescope at Kitt Peak, Arizona, in 1997 June (RAFGL 2688) and 1997 December (RAFGL 618). Phoenix illuminates a 256 × 1024 section of an Aladdin InSb detector array. The spectrograph slit was $\sim 60'' \times 1''.4$, oriented approximately east-west. The pixel scale along the dispersion axis of the spectrograph was 1.29 km s^{-1}. From the widths of OH airglow lines present in the raw spectra, we estimate the velocity resolution as $\sim$4 km s^{-1} at the time these spectra were obtained. This resolution is comparable to that of the millimeter-wave molecular line interferometry (e.g., Bieging & Rieu 1996) and represents an order-of-magnitude improvement over previous imaging spectroscopy of H_2 emission from RAFGL 2688 (Cox et al. 1997). The pixel scale in the cross-dispersion direction was 0".35, and the spatial resolution was $\sim 1''.5$.

A spectral image centered near the 2.1218 μm $S(1)$, $v = 1$–0 transition of H_2 was obtained at each of 12 spatial positions as the slit was stepped from south to north across RAFGL 2688. The step size, 1".0, provided coverage of the entire H_2-emitting region (Fig. 1) with spatial sampling approximating the slit height. For RAFGL 618, whose bright H_2 emission regions are oriented almost perfectly east-west (Latter et al. 1995)—parallel to the Phoenix slit—we obtained a single spectral image centered on the object. Integration times for both sources were 1200 s per position. Spectral images were reduced and wavelength calibrated as described by Weintraub et al. (1998). Bad pixels were removed by calculating the running mean for 7 × 7 groups of pixels and replacing outliers in each pixel group with the running mean. For the RAFGL 2688 data, the reduced spectral images were stacked in declination according to the commanded telescope offsets, to produce a (right ascension, declination, velocity) data cube of H_2 emission.

3. RESULTS

3.1. *RAFGL 2688*

3.1.1. H_2 *Position-Velocity Maps and Selected Spectra*

Calibrated spectral images of RAFGL 2688 are presented in Figure 2. All four distinct H_2 emitting regions (hereafter referred to as the north, east, south, and west lobes) seen in the NICMOS image (Fig. 1) are clearly detected in these spectral images (see, e.g., the decl. = $-1''$ panel). In addition, the large velocity gradients of molecular emission in RAFGL 2688 are readily apparent in the Phoenix data. The south lobe H_2 emission (Fig. 2, *top four panels*) is predominantly redshifted with respect to the systemic velocity of RAFGL 2688 (V_{sys}), with velocities ranging from ~ -5 to $\sim +30$ km s^{-1} relative to V_{sys}. The north lobe emission (*bottom four panels*) appears almost as a "mirror image" of the south lobe in terms of its velocity pattern, with emission predominantly at blueshifted velocities ranging from ~ -35 to $\sim +5$ km s^{-1} relative to V_{sys}. The velocity domains of the north and south lobes are well illustrated in representative spectra extracted from the images obtained at declination offsets of $+4''$ and $-4''$, respectively (Fig. 3*a*).

As expected from the known position angle (P.A.) of the polar axis of the system, P.A. $\sim 12°$ (Weintraub et al. 2000), the east lobe is detected between declination offsets of $-3''$ and $+2''$, whereas the west lobe emission is detected between offsets of $-2''$ and $+3''$. The position-velocity images obtained at these positions dramatically demonstrate the east-west velocity gradient previously detected in molecular emission-line studies of RAFGL 2688, as do representative spectra extracted from the east and west lobe emission regions in the spectral image obtained at 0" declination offset (Fig. 3*b*). That is, the east lobe is primarily blueshifted, whereas the west lobe is primarily redshifted. As we discuss in more detail below, however, the east-west and north-south velocity gradients differ in detail. In addition, the spectra in Figure 3 illustrate that the H_2 line profiles of the east and west lobes are generally narrower than those of the north and south lobes.

The Phoenix spectral images also reveal velocity structure *within* the north, south, and east lobes. In particular, the brightest emission from the south lobe is seen to migrate from lower to higher redshifted velocities, moving inward

[4] National Optical Astronomy Observatories is operated by Associated Universities for Research in Astronomy, Inc., for the National Science Foundation.

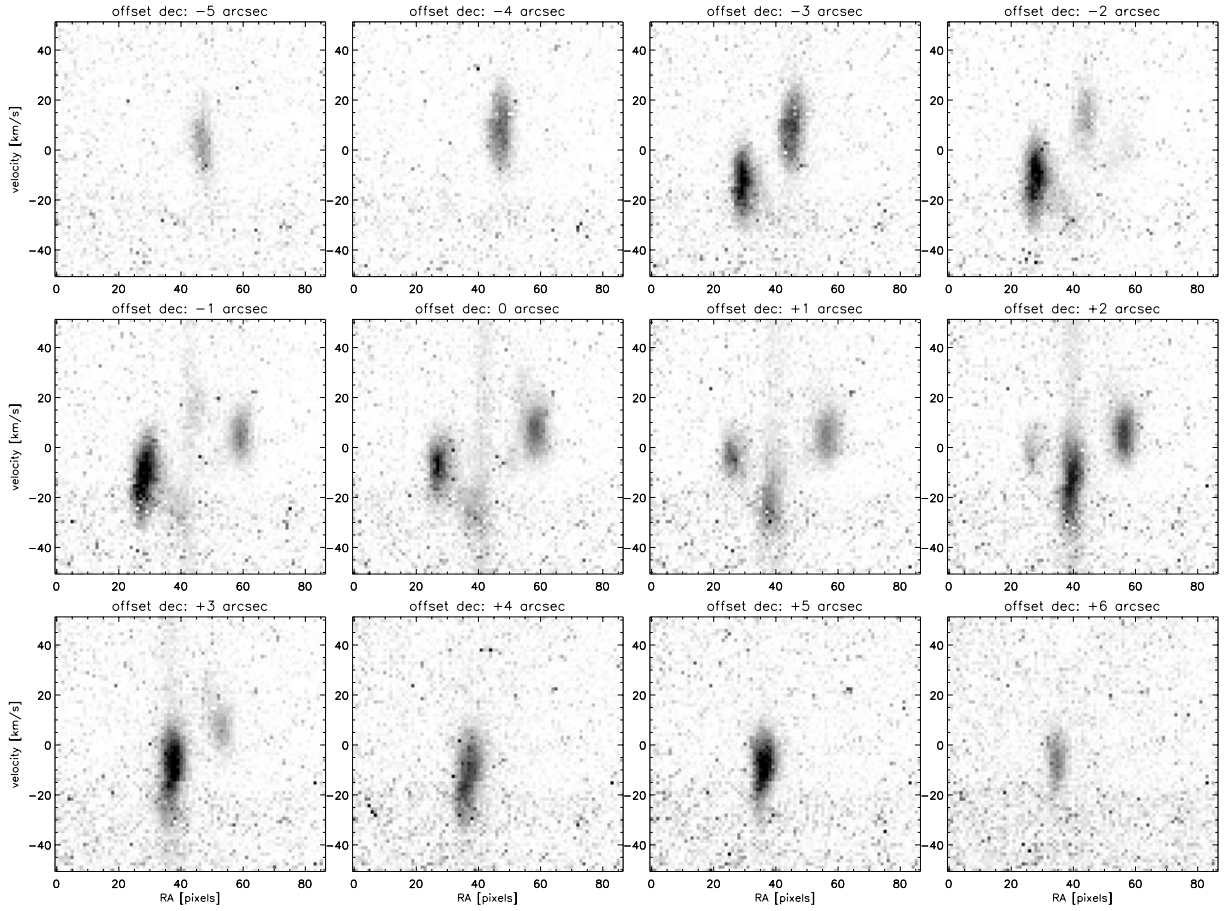

FIG. 2.—Phoenix spectral images of RAFGL 2688. Images were obtained at the declination offsets indicated above each frame. Each calibrated image is represented as a position-velocity map, with R.A. running along image columns and radial velocity running along image rows. The velocity scale of each image is centered on the systemic velocity of RAFGL 2688 with respect to the local standard of rest, $V_{sys} = -34$ km s^{-1} (e.g., Bieging & Rieu 1996). East is to the left; the spatial scale is 0.″35 pixel^{-1}, with the central star located very near pixel column 42 (nebular continuum emission is also evident in the images in the center panels). Relative intensities in these and other images presented in this paper are represented with a linear gray scale unless otherwise indicated.

(northward) from its tip at $-5''$ in decl. to $-2''$ in decl. The north lobe exhibits precisely complementary behavior, with its brightest emission migrating from lower to higher blueshifted velocities moving inward (southward) from $+6''$ in decl. to $+2''$ in decl. The east lobe also shifts in central velocity with declination offset, migrating from larger to smaller blueshifted velocities moving from south to north (i.e., from $-3''$ to $+2''$ in declination offset). In contrast, the velocity centroid of the west lobe does not shift noticeably with declination offset.

3.1.2. H_2 *Data Cube and Velocity Centroids*

In Figure 4 we display selected velocity planes from the H_2 data cube constructed for RAFGL 2688. The four principal "lobes" of H_2 emission are apparent again, with one pair oriented parallel (roughly north-south) and one perpendicular (roughly east-west) to the polar axis. The velocity gradients in the north-south and east-west H_2 lobe pairs are plainly evident in these images, with the north and east lobes blueshifted by up to ~ 25 km s^{-1} and the south and west lobes similarly redshifted. As previously mentioned, however, the north-south and east-west H_2 lobe pairs differ in their detailed kinematic signatures, as we now further describe.

The polar H_2 lobes of RAFGL 2688 each display velocity gradients along the polar axis. This velocity gradient is apparent in the velocity-resolved images of RAFGL 2688 (Fig. 4). At the most extreme blueshifted and redshifted velocity intervals, respectively, only those portions of the north and south lobes nearest the inferred position of the central star are apparent, whereas the outer regions (tips) of the lobes appear brightest at more moderate radial velocities. This trend is made more quantitative in a plot of the velocity centroid of H_2 emission as a function of position along the polar axis (Fig. 5). To construct this plot, we extracted spectra at each declination offset (see caption of Fig. 3). We then fit a Gaussian function to the H_2 line profile in each spectrum, to obtain the line velocity centroid. The resulting trend in the velocity centroids (Fig. 5) is easily anticipated based on the position-velocity images themselves (Fig. 2); i.e., relatively low velocity emission ($\sim \pm 4$ km s^{-1}) is seen at the tips of the lobes, while the highest velocity emission in each lobe ($\sim \pm 30$ km s^{-1}) is found nearest the position of the central star. This trend is remarkably similar to that observed in the position-velocity image of RAFGL 618 (§ 3.2).

In contrast, images extracted from the data cube (Fig. 4) demonstrate that the east lobe displays a gradient from north to south, perpendicular to the line joining it to the central star's position. Specifically, note that in the image centered at -26.6 km s^{-1}, only the southernmost tip of the east lobe appears, whereas in the image centered at

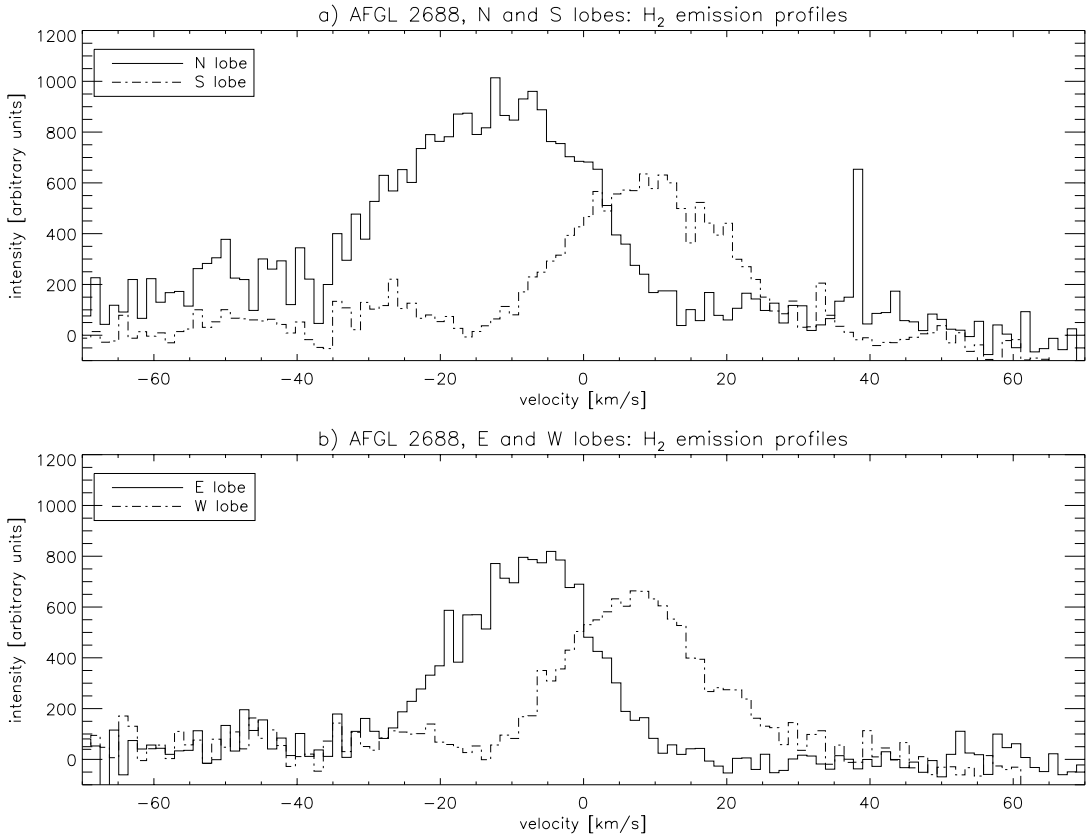

FIG. 3.—Spectra extracted (*a*) from spectral images obtained at declination offsets of $+4''$ (north lobe) and $-4''$ (south lobe) and (*b*) from spectral images obtained at $0''$ declination offset (east and west lobes). Each spectrum is obtained by summing image sections of width $4''.5$ in R.A., centered on the peak of H_2 emission. The velocity scale of each spectrum is centered on the systemic velocity of RAFGL 2688, with respect to the local standard of rest.

-0.7 km s^{-1}, the entire east lobe is present. Hence, the Phoenix data appear to resolve kinematically the distinct emission components of the east lobe that are resolved spatially in the NICMOS H_2 image of RAFGL 2688 (Fig. 1). The west lobe, meanwhile, does not reveal similar velocity structure, a result qualitatively consistent with its more localized appearance in the NICMOS image.

3.2. *RAFGL 618*

The Phoenix spectral image obtained for RAFGL 618 is displayed in Figure 6. Bright H_2 emission is detected along the entire length of RAFGL 618. Spectra extracted from this image (Fig. 7) demonstrate that very high velocity H_2 emission (up to $\sim \pm 120$ km s^{-1} in each lobe) is present in this bipolar outflow. Similarly, broadline wings have been detected previously in millimeter- and submillimeter-wave molecular spectra of RAFGL 618 (e.g., Gammie et al. 1989; Neri et al. 1992; Meixner et al. 1998). The H_2 spectra demonstrate unequivocally that—as is the case for RAFGL 2688—the highest velocity molecular material is found closest to the central star of RAFGL 618. A similar result was inferred for RAFGL 618 by Gammie et al., based on the relative strengths of line wing emission in single-dish CO (2–1) and CO (3–2) spectra.

4. DISCUSSION

4.1. *A Kinematical Model of* H_2 *Emission from RAFGL 2688*

We now construct a detailed, empirical model of the H_2 kinematics of RAFGL 2688. In formulating this model, we are guided by our observations that (1) the polar lobes are characterized by velocity gradients in which the fastest moving material is found closest to the star, and the slowest moving material is found at the tips of the H_2 emission regions; and (2) the H_2 emission seen projected along the equatorial plane contains a substantial velocity gradient east to west and a second, smaller velocity gradient in the east lobe that runs north to south.

4.1.1. *Polar Lobe* H_2 *Kinematics*

The Gaussian shapes of the spatially integrated H_2 emission-line profiles of the polar lobes of RAFGL 2688 (Fig. 3*a*) are similar to the molecular emission-line profiles detected in the radio regime from species such as CO and HCN (e.g., Bieging & Rieu 1996). The H_2 line profiles can be understood in the context of the detailed morphology of H_2 emission seen in the NICMOS image (Fig. 1). In this image the north and south lobes appear as limb-brightened cavities. The emission peaks of the line profiles correspond to the brightest regions of the lobes—their limbs (i.e., outlines)—whereas the line wings are produced by emission from within the fainter lobe interiors, which is dominated by material in the near sides (blue wings) and far sides (red wings) of the lobes.

The peak of the line profile, therefore, indicates the line-of-sight component of the H_2 velocity at the lobe limb, and we can infer the deprojected north and south lobe H_2 velocities as a function of position given an estimate of i, the inclination of the polar axis of the system out of the plane of the sky. Previous results (Yusef-Zadeh, Morris, & White 1984; Sahai et al. 1998a) suggest $i \sim 15°$. The velocities we

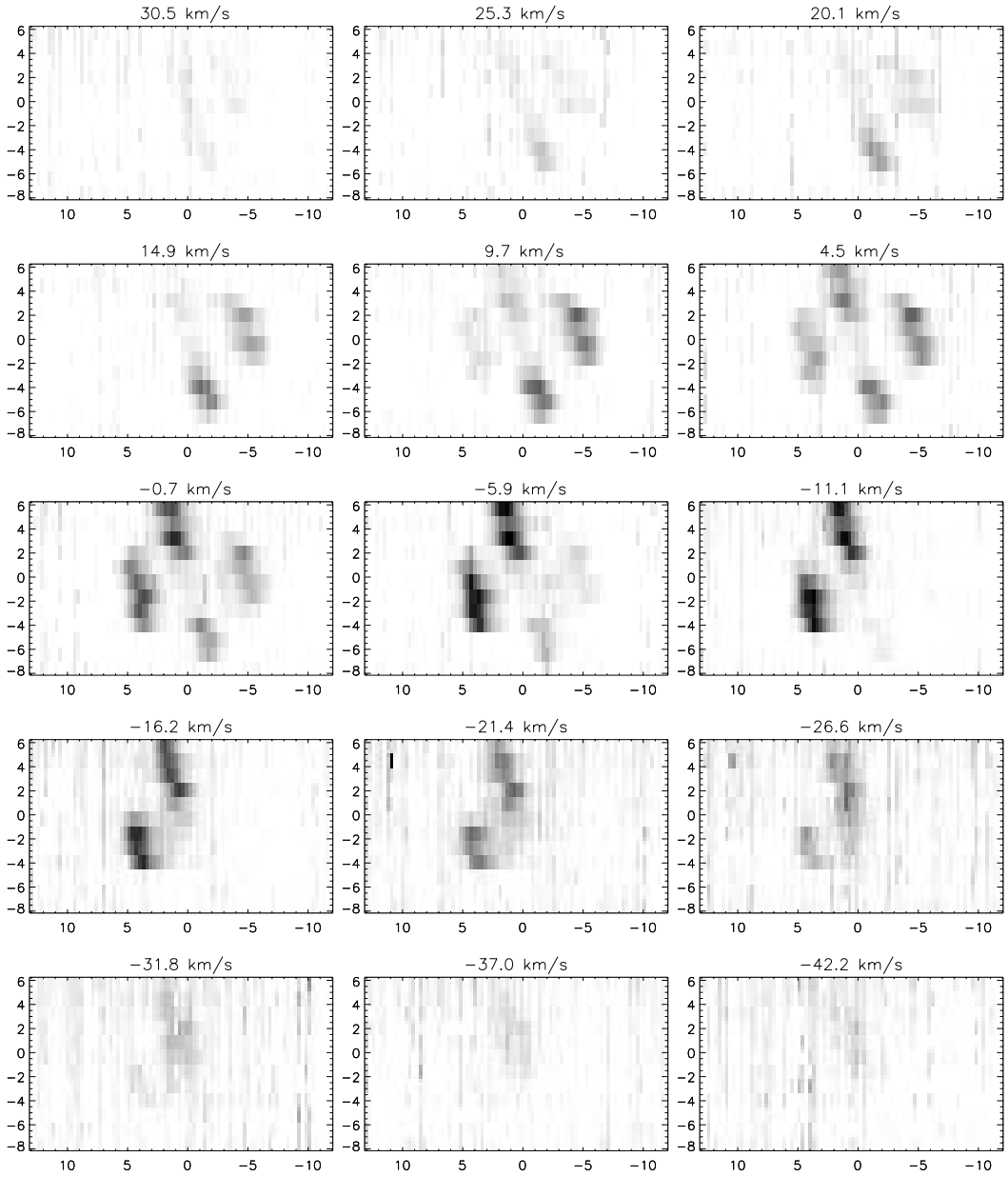

FIG. 4.—Velocity-integrated H_2 images of RAFGL 2688, extracted from the Phoenix data cube. Row and column image scales indicate offsets (arcsec) in R.A. and decl., respectively. Each image is integrated over ~ 5 km s^{-1} and is centered at the velocity indicated. These velocities are relative to the systemic velocity of RAFGL 2688.

measure at the tips of the lobes (~ 5 km s^{-1}; Fig. 5) then suggest that the gas in this region is expanding away from the central star at a velocity ~ 20 km s^{-1}. We further infer that the H_2 velocities in the regions of the lobes within $\sim 1''$ of the inferred position of the central star rise to ~ 70 km s^{-1}.

For simplicity, we assume this behavior can be described by an inverse power law of the form

$$v(\Delta\alpha, \Delta\delta) = v_0 \left(\frac{r_0}{r}\right)^p \sin i \qquad (1)$$

for (R.A., decl.) offsets ($\Delta\alpha$, $\Delta\delta$) that lie within 45° of the projected polar axis of RAFGL 2688, where v_0 is the velocity at the tips of the polar lobes, $v(\Delta\alpha, \Delta\delta)$ is the observed radial velocity at projected angular radius $r = [(\Delta\alpha)^2 + (\Delta\delta)^2]^{1/2}$ from the central star, and i is the inclination of the polar axis out of the plane of the sky. Based on the foregoing discussion of line profiles, we make the further simplification that the polar H_2 emission is dominated by emission from the lobe limbs.

4.1.2. *Equatorial Plane* H_2 *Kinematics*

If one postulates that all of the east-west H_2 *emission is confined to a narrow region along the equatorial plane*, then a component of azimuthal velocity must be present in the material responsible for this emission. Such a structure might be analogous to that of the equatorial "skirt" observed in η Car (Smith, Gehrz, & Krautter 1998). Although the kinematics of the two objects appear to differ

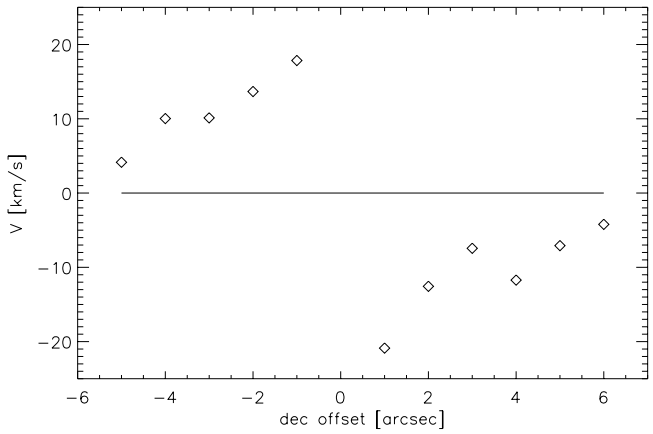

FIG. 5.—Radial velocity centroid, with respect to systemic velocity, of H_2 emission vs. position along the polar axis of RAFGL 2688. Uncertainties in determinations of velocity centroids are approximately the symbol size.

in detail (Zethson et al. 1999), the H_2 morphology in the NICMOS image (Fig. 1) is consistent with the confinement of the H_2-emitting material in RAFGL 2688 to the plane of the system: knot E2 is brighter than knot E4, as expected if the former is directed toward the observer and the latter is directed away from the observer, while E1 and E3, which mark the perpendiculars to the polar axis (see Weintraub et al. 2000, their Fig. 6), are of similar intensity, as expected if we view these structures through similar columns of intervening material.

We therefore assume that the equatorial plane H_2 kinematics consist of a combination of azimuthal (rotation) and radial (expansion) velocity components. We calculate these velocities from the relation

$$v(\Delta\alpha, \Delta\delta) = (v_e \sin \phi + v_r \cos \phi) \cos i \qquad (2)$$

for (R.A., decl.) offsets $(\Delta\alpha, \Delta\delta)$ that lie within 45° of the projected equatorial plane of RAFGL 2688, where v_e is the expansion velocity, v_r is the rotational velocity about

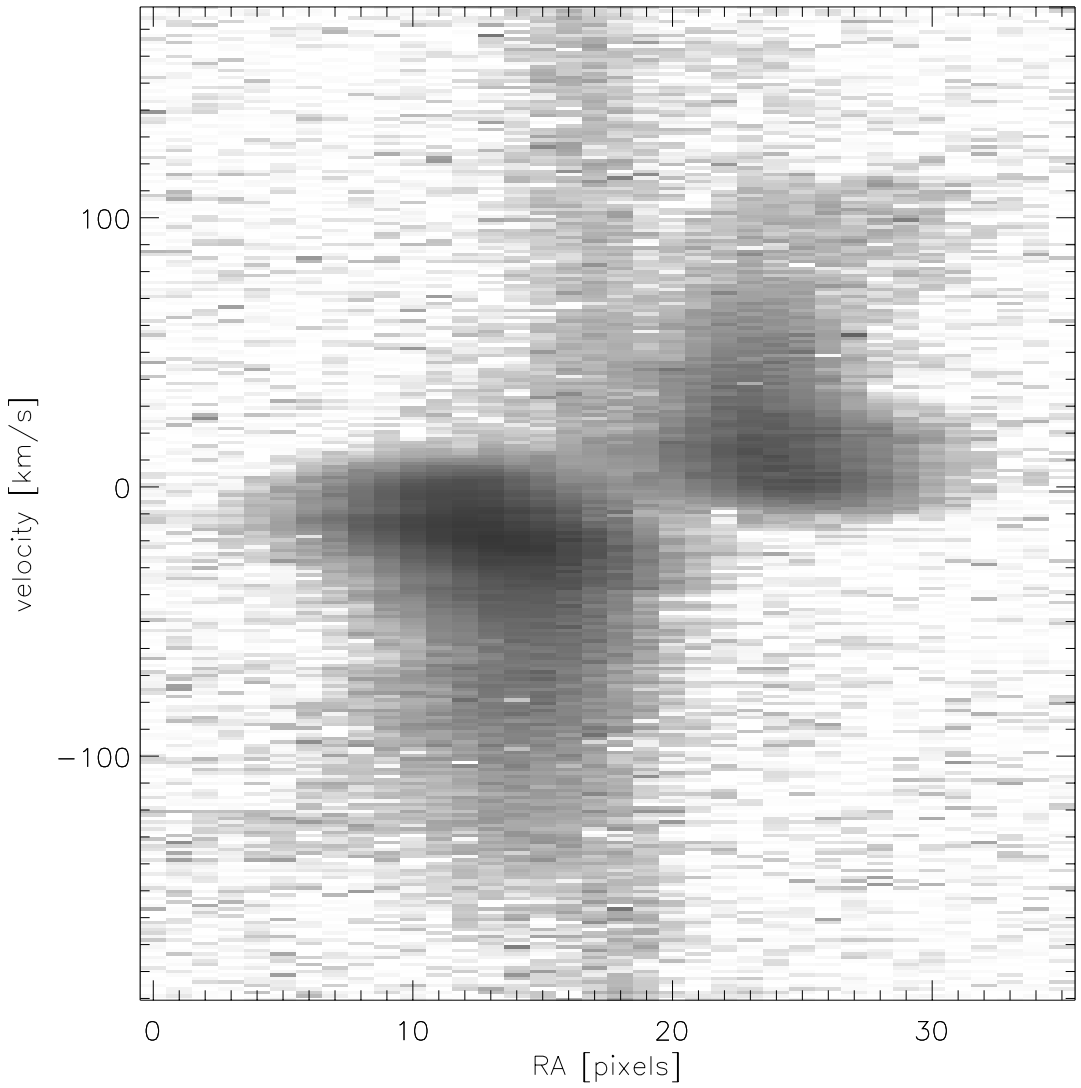

FIG. 6.—Calibrated Phoenix spectral image of RAFGL 618. The velocity scale of the image is centered on the systemic velocity of RAFGL 618. East is to the left; the spatial scale is 0″.35 pixel^{-1}, with the central star located very near pixel column 18 (continuum emission is present at this position in the form of vertical band across the image). The image is displayed in a logarithmic gray scale to bring out the faint line-wing emission, which extends to $\sim \pm 120$ km s^{-1}.

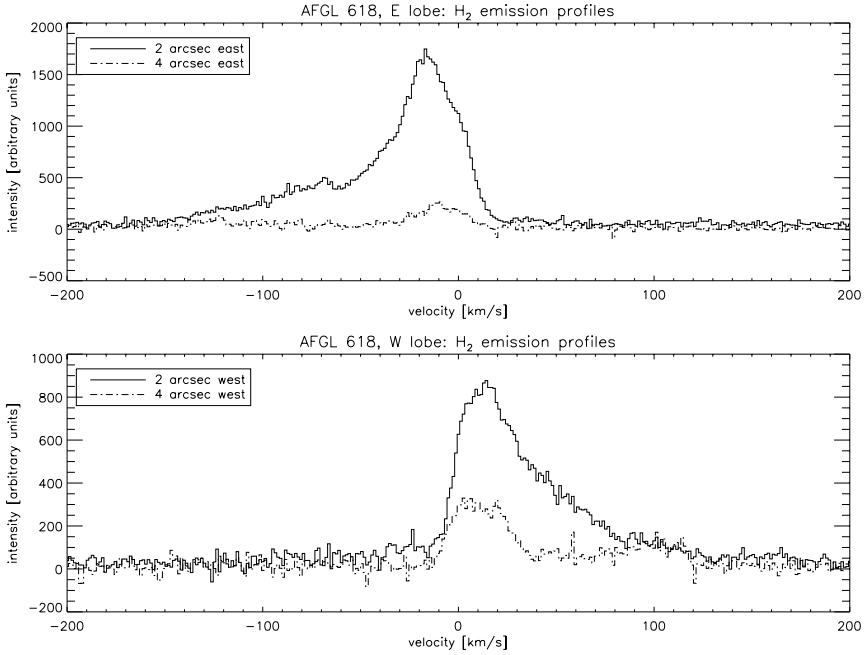

FIG. 7.—Spectra extracted from the spectral image of RAFGL 618. Each spectrum is obtained by summing image sections of width 2″ in R.A. at the offset indicated. The velocity scale of each spectrum is centered on the systemic velocity of RAFGL 618 with respect to the local standard of rest (-21 km s^{-1}; e.g., Meixner et al. 1998).

the polar axis, and ϕ is the azimuthal angle with respect to the polar axis of RAFGL 2688, given by

$$\phi = \tan^{-1}\left(\frac{\Delta x}{\Delta y \sin i}\right). \quad (3)$$

Offsets (Δx, Δy) are then related to ($\Delta\alpha$, $\Delta\delta$) via a rotation of the coordinate system by the projected position angle of the polar axis on the plane of the sky.

4.1.3. *Comparison with Data*

Model parameters v_0 and p are relatively well constrained by Figure 5, from which we infer $v_0 \sim 20$ km s^{-1} and $p \sim 0.7$. It is more difficult to constrain the values of the parameters governing the equatorial plane H_2 radial velocities, v_e and v_r. To do so, we compared model velocity field images [$v(\Delta\alpha, \Delta\delta)$] calculated for a range of values of v_e and v_r, with velocity centroids calculated from the Phoenix data cube (see, e.g., Bieging & Rieu 1996). We find qualitative and rough quantitative agreement between model and data for values of both v_e and v_r in the range 5–10 km s^{-1}, with the additional constraint $v_e + v_r \sim 15$ km s^{-1}. An example of the results for a representative successful model is displayed in Figure 8. In this figure the model velocity centroid image is calculated from equations (1) and (2) for values of $v_e = 5$ km s^{-1} and $v_r = 10$ km s^{-1}. There is clear qualitative agreement between the model and observed velocity images for these parameter values, in the sense that the overall distribution of redshifted and blueshifted emission is captured by the model. Furthermore, this model reproduces the important details of the observed H_2 velocity distribution previously described. Specifically, the model recovers the magnitudes and positions of the observed blueshifted velocity extrema near (R.A., decl.) offsets ($+1''$, $+2''$) in the north lobe and ($+5''$, $-3''$) in the east lobe, as well as the magnitudes and positions of redshifted velocity extrema near offsets ($-1''$, $-2''$) in the south lobe and at ($-4''$, $+3''$) in the west lobe.

Empirically, we find these parameter values—$v_0 = 20$ km s^{-1}, $p = 0.7$, $v_e = 5$–10 km s^{-1}, and $v_r = 5$–10 km s^{-1}—provide the best agreement between model and data in terms of overall qualitative appearance of the velocity images as well as in the location *and* magnitude of the velocity extrema. However, this model cannot be considered a "best fit" to the data. Rather, the foregoing comparison of calculated and observed velocity fields offers an indication of the magnitude of an azimuthal velocity component relative to the components of radial expansion both parallel and perpendicular to the polar axis.

4.2. *Alternative Models*

The kinematic model described in § 4.1 is not unique. For example, on the basis of high spatial and spectral resolution CO maps, which display kinematics very similar to those seen in H_2 emission, Cox et al. (1997, 2000) and Lucas et al. (2000) have proposed that the velocity gradients parallel and perpendicular to the polar axis result from a multipolar system of jets whose directions of motion are everywhere directed radially outward from the central star. Since the entire fanlike eastern H_2 emission region is blueshifted, the Cox et al. model requires that these outflows must be directed well "above" the equatorial plane of the system toward the observer, while the outflows responsible for the western H_2 emission region are more tightly confined and directed "below" the equatorial plane, away from the observer. Hence, in this model, the remarkable orthogonality of the H_2 and CO emission morphologies is purely a result of viewing angle. Multiple symmetry axes are also suggested by observations of radio continuum emission (Jura et al. 2000). Chaotic precession of bipolar jets might explain these observations (see, e.g., Livio 2000 and references therein). The very similar linear extents of the orthogonal north-south and east-west molecular emission regions appear to pose a problem for any model invoking precessing jets, however.

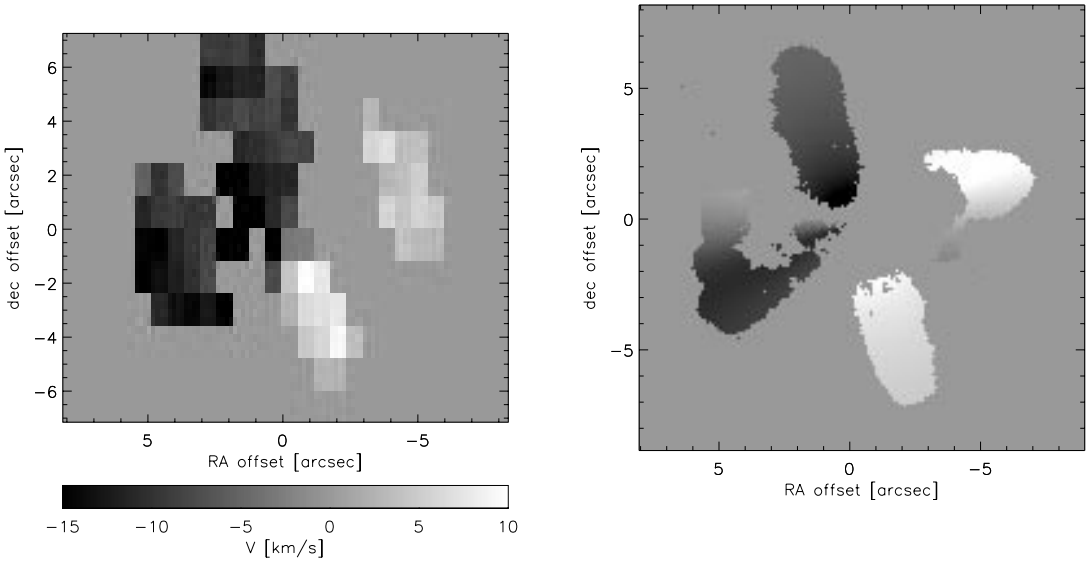

FIG. 8.—Comparison of observed and model H_2 velocity fields for RAFGL 2688. The observed velocity field (*left*) consists of velocity centroids calculated from the Phoenix data cube. In the model (*right*), we set the equatorial expansion velocity at $v_e = 5$ km s^{-1} and the equatorial rotation velocity at $v_r = 10$ km s^{-1} (see § 4.1.3). We display only those portions of the model velocity image for which the signal-to-noise ratio in the *HST*/NICMOS H_2 image exceeds ~ 5 and only those portions of the observed velocity centroid image for which the signal-to-noise ratio in the velocity-integrated Phoenix H_2 image exceeds ~ 3.

Bieging & Rieu (1988, 1996) have proposed a model in which the radio molecular line emission from the projected equatorial plane of RAFGL 2688 originates in an expanding, rotating equatorial disk or torus. Though qualitatively similar to the model proposed in § 4.1, our model does not require that the H_2 emission arises from a disk. Rather, the east-west H_2 lobes, like the polar (north-south) H_2 lobes (see below), trace the interaction between material ejected along the equatorial plane at two different epochs; indeed, the interferometric radio molecular line observations indicate that the molecular jets detected in CO may be responsible for shocks that produce the H_2 emission, based on the striking correspondence between the CO and H_2 emission morphologies (Lucas et al. 2000). There is no particular reason to assume that the previously ejected material forms a complete torus around the star and, indeed, Cox et al. (2000) and Morris & Sahai (2000) have argued, on the basis of radio and mid-infrared imaging, respectively, that no such structure exists. However, the optical and infrared morphology of the nebula—in particular, the apparent occultation of the southern H_2 lobe and reflection nebulosity within $\sim 2''$ of the central star—does suggest the presence of a large ($\sim 5''$ radius), optically thick structure.

4.3. *Origin of the Shocked* H_2 *Emission*

4.3.1. *The Transition from Spherical to Axial Symmetry*

As noted by Sahai et al. (1998a), the detailed morphology of near-infrared H_2 emission from RAFGL 2688 strongly supports previous suggestions that the emission arises in shocks formed by the interaction of recently developed, fast-moving winds with slower moving material. This relatively slow-moving material likely was ejected during the AGB phase of the progenitor star. Assuming J-type shocks are the origin of the gas heating that leads to H_2 emission then, according to model calculations (e.g., Burton, Hollenbach, & Tielens 1992), the shock fronts at the H_2 lobe tips are moving at a minimum velocity $v_s \sim 10$ km s^{-1} in the frame of the preshocked (AGB) wind. This limit corresponds roughly to the energy threshold for excitation of the $v = 1$–0 $S(1)$ H_2 line. Hence, if the velocities inferred for the tips of the polar lobes and for the equatorial region, ~ 20 and ~ 15 km s^{-1}, respectively, consist of a superposition of (minimum) shock and AGB wind velocities, we infer that the AGB wind was ejected at $v_{\rm AGB} \sim 5$–10 km s^{-1}, which is typical of *low-mass* carbon stars. On the other hand, the nascent bipolar structure and strong H_2 emission of RAFGL 2688 hint at a relatively massive progenitor (Kastner et al. 1996) which may, in turn, suggest a larger AGB outflow velocity ($v_{\rm AGB} \sim 20$ km s^{-1}; e.g., Kastner et al. 1993). If so, it would appear that, at their leading edges, the shocks which excite H_2 have imparted very little momentum to the former AGB wind. In either case it is apparent that, well behind the leading edges of the shocks that excite the H_2 in the polar lobes, considerable wind acceleration has taken place. The maximum speed for non-dissociative shocks is ~ 25 km s^{-1} (Burton et al. 1992). Thus, within $\sim 1''$ (~ 1000 AU) of the central star of RAFGL 2688, the outflow velocity of the gas is at least ~ 45 km s^{-1}, which is much larger than the outflow velocities of AGB stars. In RAFGL 618, meanwhile, the inferred polar outflow velocities very near the central star are at least ~ 100 km s^{-1} (neglecting projection effects), assuming the shocks are traveling at ~ 25 km s^{-1}.

We conclude that the velocity gradients along the polar axes of both RAFGL 2688 and RAFGL 618 trace rapid transitions from the "slow," spherically symmetric winds of their AGB progenitors to faster, collimated, post-AGB winds. A likely mechanism for such a transition is that late AGB and post-AGB ejecta relatively close to the central star are accelerated with increasing efficiency as the star is "unveiled" and circumstellar material is exposed to a progressively hotter photosphere and, potentially, a stronger stellar magnetic field. Indeed, RAFGL 2688 has been observed to be increasing steadily in optical magnitude (Gottlieb & Liller 1976). These conditions would appear to be conducive to the formation of H_2 shocks during the post-AGB but pre–planetary nebula phase of bipolar nebulae, a scenario consistent with the conclusions of Wein-

traub et al. (1998). Such shocks could then play a central role in the transition from spherically symmetric to axisymmetric outflow, as the "young," fast (but still predominantly molecular) wind driven by the emerging post-AGB star excavates bipolar cavities within the previously ejected red giant wind. The displacement from the central star to the tips of the H_2 lobes ($\sim$6000 AU), combined with the deprojected velocities at the lobe tips, $v_0 \sim 20$ km s^{-1}, suggests the H_2 lobes have a dynamical age of 1500 yr, which then serves as an upper limit to the post-AGB "unveiling" of the central star.

4.3.2. *The Egg Nebula as Endpoint of Common Envelope Binary Evolution*

A presently popular theory accounts for the structure of bipolar planetary nebulae as due to the interaction of a close binary system, in which the secondary diverts mass loss from and/or spins up the envelope of the primary (e.g., Soker 1997, 1998). According to a specific formulation of the binary progenitor model (Soker 1998), the relatively massive progenitors of bipolar PNs undergo a phase during the AGB evolution of the primary in which the secondary resides just outside the envelope of the primary and diverts mass loss into the equatorial plane. This phase is followed by a short-lived common envelope phase that, presumably, rapidly spins up the envelope of the primary; the carbon star V Hya, which displays $V \sin i \sim 13$ km s^{-1}, may be undergoing such a phase at present (Barnbaum, Morris, & Kahane 1995).

Many, though certainly not all, of the observed characteristics of RAFGL 2688 appear to be explained by such a model. Specifically, its notorious system of concentric broken arcs would result from episodic, spherically symmetric mass loss during a prolonged period of quasi–single-star AGB mass loss preceding the common envelope phase; the subsequent formation of bipolar structure would be the result of the increasingly close proximity of a companion during the late-AGB evolution of the primary; and the H_2 shocks would mark the rapid termination of a common envelope phase and the resultant sudden ejection of the remaining AGB star envelope. Hence, the H_2 emission regions are produced by bullet-like ejecta that have collided with material that was recently ejected—much of it along the equatorial plane—during the close binary phase preceding common envelope formation.

It would appear that no existing model can explain satisfactorily the rich phenomenology of the Egg Nebula. The molecular kinematics of its equatorial region remain particularly problematic for present models, whether or not a component of azimuthal velocity is present along the equatorial plane of the system. A pure radial outflow model cannot explain the striking orthogonality of the molecular emission from RAFGL 2688; furthermore, such a model is, at present, reliant on ad hoc physical mechanisms for the presence of multiple symmetry axes (e.g., Frank 2000). On the other hand, the azimuthal velocities of the equatorial H_2 emission suggested by our model and the models of Bieging & Rieu (1988, 1996) are far too large to be explained by Keplerian rotation; an alternative source of angular momentum is required. As proposed by Bieging & Rieu, this angular momentum might be provided by magnetic fields that are corotating with the star. It is of considerable importance to establish whether sufficiently large fields can be generated via interaction with a close companion star (Bieging & Rieu 1988, 1996) or by dynamo activity in the primary post-AGB star itself (e.g., Soker 2000; Blackman, Frank, & Welch 2000). The latter mechanism could be particularly effective if the central star has just undergone a common envelope phase, such that highly magnetically active interior layers of the star drive the molecular jets seen in CO and H_2.

Support for this research was provided in part by a JPL/*ISO* grant to R. I. T. We acknowledge enlightening discussions with Adam Frank and Robert Lucas and the helpful comments of the referee.

REFERENCES

Barnbaum, C., Morris, M., & Kahane, C. 1995, ApJ, 450, 862
Bieging, J., & Rieu, N.-Q. 1988, ApJ, 324, 516
———. 1996, AJ, 112, 706
Blackman, E., Frank, A., & Welch, C. 2000, ApJ, submitted (astro-ph/0005288)
Burton, M. G., Hollenbach, D. J., & Tielens, A. G. G. M. 1992, ApJ, 399, 563
Cox, P., Lucas, R., Huggins, P. J., Forveille, T., Bachiller, R., Guilloteau, S., Mallard, J. P., & Omont, A. 2000, A&A, 353, L25
Cox, P., et al. 1997, A&A, 321, 907
Frank, A. 2000, in ASP Conf. Ser. 199, Asymmetrical Planetary Nebulae II: From Origins to Microstructures, ed. J. H. Kastner, N. Soker, & S. A. Rappaport (San Francisco: ASP), 225
Gammie, C., Knapp, G. R., Young, K., Phillips, T. G., & Falgarone, E. 1989, ApJ, 345, L87
Gatley, I., Depoy, D. L., & Fowler, A. M. 1988, Science, 242, 1264
Gottlieb, E. W., & Liller, W. 1976, ApJ, 207, L135
Hinkle, K. H., Cuberly, R., Gaughan, N., Heynssens, J., Joyce, R., Ridgway, S., Schmitt, P., & Simmons, J. E. 1998, Proc. SPIE, 3354, 810
Jura, M., Turner, J. L., Van Dyk, S., & Knapp, G. 2000, ApJ, 528, L105
Kastner, J. H., Forveille, T., Zuckerman, B., & Omont, A. 1993, A&A, 275, 163
Kastner, J. H., Weintraub, D. A., Gatley, I., Merrill, K. M., & Probst, R. P. 1996, ApJ, 462, 777
Kastner, J. H., Soker, N., & Rappaport, S.A., eds. 2000, Asymmetrical Planetary Nebulae II: From Origins to Microstructures (San Francisco: ASP)
Latter, W. B., Kelly, D. M., Hora, J. L., & Deutsch, L. K. 1995, ApJS, 100, 159
Livio, M. 2000, in ASP Conf. Ser. 199, Asymmetrical Planetary Nebulae II: From Origins to Microstructures, ed. J. H. Kastner, N. Soker, & S. A. Rappaport (San Francisco: ASP), 243
Lucas, R., Cox, P., & Huggins, P. J. 2000, in ASP Conf. Ser. 199, Asymmetrical Planetary Nebulae II: From Origins to Microstructures, ed. J. H. Kastner, N. Soker, & S. A. Rappaport (San Francisco: ASP), 285
Meixner, M., Campbell, M. T., Welch, W. J., & Likkel, L. 1998, ApJ, 509, 392
Morris, M., & Sahai, R. 2000, in ASP Conf. Ser. 199, Asymmetrical Planetary Nebulae II: From Origins to Microstructures, ed. J. H. Kastner, N. Soker, & S. A. Rappaport (San Francisco: ASP), 143
Neri, R., Garcia-Burillo, S., Guelin, M., Cernicharo, J., Guilloteau, S., & Lucas, R. 1992, A&A, 262, 544
Ney, E. P., Merrill, K. M., Becklin, E. E., Neugebauer, G., & Wynn-Williams, C. G. 1975, ApJ, 198, L129
Sahai, R., Hines, D., Kastner, J. H., Weintraub, D. A., Trauger, J. T., Rieke, M. J., Thompson, R. I., & Schneider, G. 1998a, ApJ, 492, 163L
Sahai, R., et al. 1998b, ApJ, 493, 301
Smith, N., Gehrz, R. D., & Krautter, J. 1998, AJ, 116, 1332
Soker, N. 1997, ApJS, 112, 487
———. 1998, ApJ, 496, 833
Soker, N. 2000, in ASP Conf. Ser. 199, Asymmetrical Planetary Nebulae II: From Origins to Microstructures, ed. J. H. Kastner, N. Soker, & S. A. Rappaport (San Francisco: ASP), 71
Weintraub, D. A., Huard, T., Kastner, J. H., & Gatley, I. 1998, ApJ, 509, 728
Weintraub, D. A., Kastner, J. H., Sahai, R., & Hines, D. 2000, ApJ, 531, 401
Westbrook, W. E., Becklin, E. E., Merrill, K. M., Neugebauer, G., Schmidt, M., Willner, S. P., & Wynn-Williams, C. G. 1975, ApJ, 202, 407
Yusef-Zadeh, F., Morris, M., & White, R. L. 1984, ApJ, 278, 186
Zethson, T., Johansson, S., Davidson, K., Humphreys, R. M., Ishabashi, K., & Ebbets, D. 1999, A&A, 344, 211